



Vortex ring state of a shrouded rotor: an experimental survey

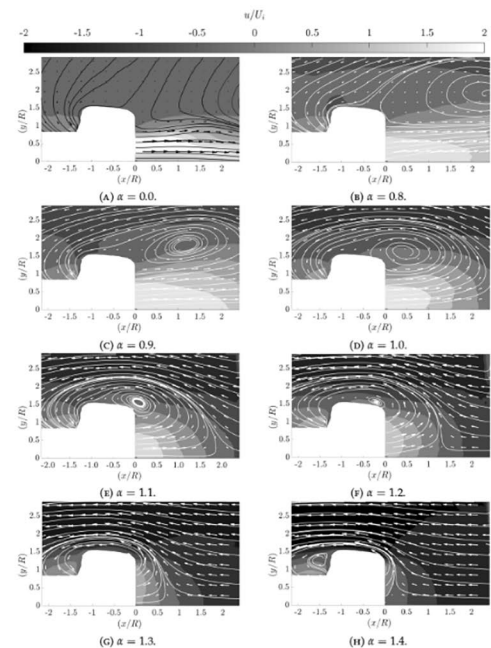
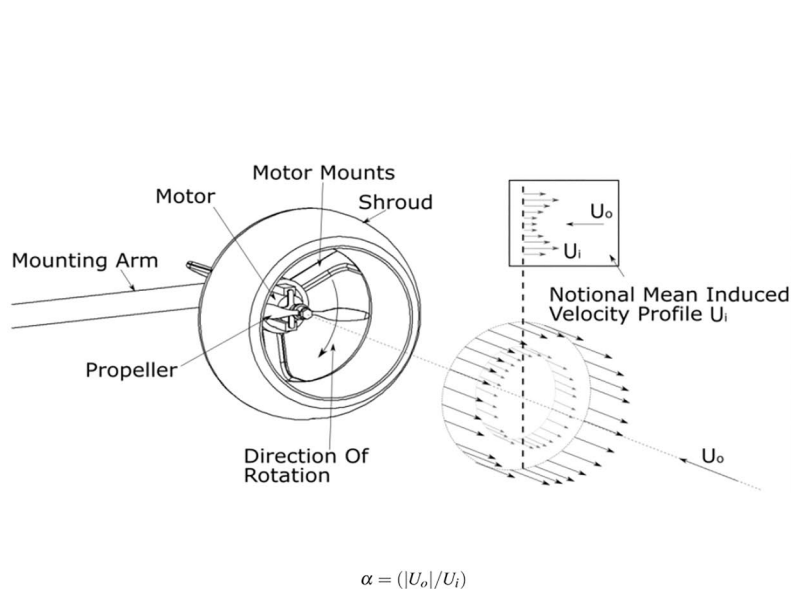
David J. Pickles¹ · Daniele Zagaglia¹ · Angela Busse¹ · Richard B. Green¹

Received: 1 August 2022 / Revised: 31 January 2023 / Accepted: 21 February 2023
© The Author(s) 2023

Abstract

The vortex ring state (VRS) is a flow condition typical of rotors operating in axial descent flight which may lead to large unpredictable thrust oscillations and possibly the loss of control of the rotorcraft. Despite the dangers associated with this flight condition, there is a distinct lack of detailed experimental data related to shrouded rotors operating in axial descent, which is of relevance owing to the number of novel unmanned aerial vehicles that incorporate this technology. This manuscript presents an experimental investigation designed to assess if and how the presence of the shroud affects the development of the vortex ring state. To this end, laser Doppler anemometry and particle image velocimetry were used to investigate the flow for a range of descent velocities and results were compared with those obtained without the shroud. Time-averaged data were used to assess the general structures of the flow fields, whilst statistical analysis of the velocity fluctuations and modal analysis of the velocity field using proper orthogonal decomposition highlighted the unsteady features of the flow. The investigation showed that shrouded rotors enter the VRS similarly to their isolated counterparts, and the presence of the shroud may be responsible for a slight delay of its onset.

Graphical abstract



✉ Daniele Zagaglia
daniele.zagaglia@glasgow.ac.uk

David J. Pickles
david.pickles@glasgow.ac.uk

¹ James Watt School of Engineering, University of Glasgow,
Glasgow, Scotland

1 Introduction

Shrouded rotors have been extensively used in the rotorcraft industry, for example, in compound helicopters for auxiliary propulsion, hovercraft, helicopter tail rotors (Mouille 1970; Vuillet and Morelli 1986), fan in wing aircraft and vertical take-off and landing (VTOL) unmanned aerial vehicles (UAVs) (Colin et al. 2016). This is due to their inherent safety (Young et al. 2002), the potential static performance (Hubbard 1950) and noise (Heller 1997) improvements when compared to an isolated rotor.

Since the initial patent application by Hamel (1923), which describes a fixed wing aircraft with propellers embedded inside the wings perpendicular to the wing chord, most of the experimental and numerical investigations on shrouded rotors have focused on characterising their performance varying several geometry parameters, such as the blade tip clearance, δ_{tip} , (Hubbard 1950; Taylor 1958), the inlet lip radius, r_{lip} , (Krüger 1949; Graf et al. 2008), the diffuser angle, θ_d , (Black et al. 1968), the diffuser length, L_d , and the diffuser expansion ratio, $\sigma_d = A_e/A$, which is defined as the ratio between the diffuser exit area, A_e , and the rotor disc area, A .

Research involving the flow produced by shrouded rotors has mainly focused on hover and edgewise flight. In hover, a shrouded rotor produces a more uniform velocity wake compared to that of an isolated rotor. The uniformity of the wake was found by Pereira (2008) to depend on the rotor blade tip clearance. Shrouded rotors with larger blade tip clearances produce wakes which closely resemble that of wakes produced by isolated rotors. Smoke flow visualisations, performed by Krüger (1949), showed that the diameter of the wake produced by a shrouded rotor was dependent on the shape of the shroud. Hot wire anemometry surveys performed by Martin and Tung (2004) showed that the diameter of the wake remains constant after it exits from the diffuser if the flow has become fully expanded at the diffuser exit plane. Quantitative PIV measurements and computational simulations of the flow field produced by a shrouded rotor UAV operating in edgewise flight were performed by Akturk et al. (2009) and Ryu et al. (2017). In edgewise flight, the effective breathing area of the rotor reduced as a result of flow separating from the leading edge of the shroud's inlet. The wake of the shrouded rotor impinged upon the rotor centre body. Pressure measurements showed that a large increase in suction pressure is produced on the windward side of the shroud, and a large suction force is produced on the leeward side of the shroud (Pereira 2008).

Whilst a large amount of data exists regarding the effect shroud design parameters have on the performance and the

structure of the flow field produced by shrouded rotors operating in hover and edgewise flight, there is a lack of detailed experimental or numerical data related to shrouded rotors operating in axial descent. This flight condition is particularly interesting since it represents a significant region of the flight envelope of UAVs, especially when operating in confined spaces or urban environments.

In axial descent, unshrouded rotors can experience a flow phenomenon known as the vortex ring state (VRS), first identified by Bothezat (1919). When operating in axial descent the system of intertwined helical vortices trailing from the rotor blades collapses leading to the formation of a highly unsteady vortex ring of a similar scale to the rotors diameter. The build-up and subsequent shedding of the vortex ring, which occurs over a number of rotor revolutions, leads to large unpredictable thrust oscillations, the loss of control efficiency and, in some cases, the loss of the rotorcraft (Reeder and Gustafson 1949; Brotherhood 1949).

The mechanism by which the trailed vortex system collapses into the toroidal form associated with the VRS is based on the linear stability analysis of helical vortex filaments performed by Gupta and Loewy (1974) along with the free wake simulations of helicopter rotors operating in axial descent conducted by Bhagwat and Leishman (2000), Leishman et al. (2004), and Ananthan and Leishman (2006). These investigations showed that the wake from a hovering rotor is inherently unstable and that the small geometric perturbations to the helix and the mutual-inductance instability of helical vortices lead to the breakdown of the helical structure. Typically, this occurs some distance away from the rotor; however, in descending flight, this occurs in the vicinity of the rotor. The mutual-inductance instability is responsible for the bundling of vortex filaments into rings, which move towards the rotor as it approaches the VRS. Outboard of the rotor, this leads to the build-up of vorticity around the rotor blade tips (Savas et al. 2009). The build-up and subsequent shedding of the recirculation is responsible for the large thrust fluctuations associated with rotors operating in the VRS.

Quantitative PIV measurements of the flow field produced by a model rotor operating in axial descent, performed by Green et al. (2005), showed that at low descent velocities the rotor wake penetrates into the counter flow and can be divided into two main regions: near and far fields. In the near field, the structure of the flow is similar to that of a hovering rotor. In the far field, as the velocity of the rotor wake decays, the rotor wake interacts with the counter flow forming a stagnation point on the geometric centre line of the rotor and a region of recirculating flow outboard of the rotor. At a descent velocity approximately equal to

the hover-induced velocity of the rotor, the flow forms an axisymmetric vortex ring in the vicinity of the rotor, which can shed aperiodically into the free stream. This is coupled with the formation of a conical region of reverse flow which can penetrate through the rotor hub (Brinson 1998; Drees and Hental 1951). The region of the rotor which experiences this reversed flow increases until the rotor enters the windmill break state. Proper orthogonal decomposition (POD) of the flow field produced by a rotor in axial descent (Green et al. 2005) indicated that in this operating condition the flow intermittently switches between that of a hovering rotor and the toroidal form associated with the VRS. The frequency with which the flow entered the VRS topology increased as the descent rate increased until the flow remained locked within the toroidal form.

As previously stated, despite the dangers associated with such flight conditions, there is a distinct lack of detailed experimental or numerical data related to shrouded rotors operating in axial descent. This manuscript presents an experimental investigation designed to assess if and how the presence of the shroud affects the development of the vortex ring state. To this end, LDA and PIV were used to investigate the flow for a range of descent velocities and results were compared with those obtained without the shroud. Time-averaged data were used to assess the general structures of the flow fields, whilst statistical analysis of the velocity fluctuations and modal analysis of the velocity field using proper orthogonal decomposition (POD) highlighted the unsteady features of the flow.

2 Experimental setup

2.1 Description of the shrouded rotor model

The experimental investigation utilised a 0.1778 m diameter, two bladed, twisted, tapered, fixed pitch rotor with a solidity of $\sigma = 0.097$ mounted inside a shroud. In order to allow the influence of the shroud on the flow field to be characterised, the flow field produced by the unshrouded rotor was also investigated. Figure 1 shows the chord (c), thickness (t) and blade pitch distribution of the blade. The rotor had no cyclic input, and there were no lead-lag or flap degrees of freedom. The fibreglass rotor was lightly loaded ($c_T/\sigma = 0.041$, as it will be estimated in Sect. 3.1.1) and therefore was assumed to be rigid. The rotor was powered by an AXI-2820/12-V2 brushless motor which was mounted on a stand located inside the wind tunnel. The shroud was connected to the motor using three support struts located on the inlet side of the rotor, as shown in Fig. 2. The rotor was operated at a constant rotational frequency of 3980 ± 2 RPM (66.3 Hz), producing a rotor tip speed of $V_{tip} = 37$ m/s and a blade tip Reynolds number of 15,000.

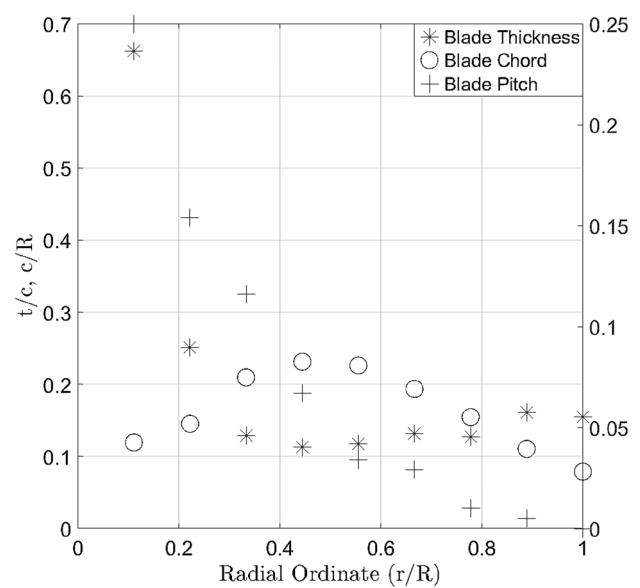


Fig. 1 Chord, thickness, and pitch profiles of the rotor blade used in this investigation

The shroud, shown in Fig. 2, was 3D printed out of Prototyping PLA (FDM) and was designed based on the investigation performed by Pereira (2008) to optimise the hovering performance of a shrouded rotor. The shroud had an inlet lip radius of $r_{lip} = 0.13D_t = 0.02$ m, a blade tip clearance ($\delta_{tip} \approx 1$ mm), a diffuser angle $\theta_d = 10^\circ$, and a diffuser length of $L_d = 0.5D_t = 0.089$ m. The rotor disc plane was located at the throat of the shroud. Rather than a single surface, inner wall-only shroud, which is characteristic of shrouds used in earlier investigations to characterise the performance of hovering shrouded rotors, a smooth curve was used to describe the external profile of the shroud. A schematic diagram of the shrouded rotor installed in the wind tunnel is shown in Fig. 3. The shrouded rotor was orientated to induce velocity (U_i) against the wind tunnel, so that the wind tunnel speed (U_o) represented the descent velocity of the shrouded or unshrouded rotor.

A Cartesian (x, y, z)-coordinate system, with its origin at the geometric centre of the shroud outlet plane, is defined so that the y -axis is vertically upwards and the x -axis is orientated against the direction of the wind-tunnel free stream. The counterflow was produced using University of Glasgow's DeHavilland wind tunnel. This atmospheric closed-return, low-speed wind tunnel is capable of achieving speeds of up to $|U_o| = 50$ m/s in the 2.65 m wide by 2.04 m high octagonal test section with a turbulence intensity below 0.4%. The shrouded and unshrouded rotors were both exposed to a range of descent velocities ranging from $\alpha = (|U_o|/U_i) = 0$ to $\alpha = 2$. The test rig shown in Fig. 3 had a negligible wind tunnel blockage of 2%.

velocities, 218 data points along two lines aligned with the horizontal (z) and vertical (y) directions, respectively, were sampled for a period of 10 s with a spatial resolution of $0.08R$ on the same plane of investigation detailed earlier. For every point, the u and v components of the velocity vector were measured, u corresponded to the rotor axial velocity, whereas v corresponded to the radial velocity when moving along the y -axis and to the tangential velocity when moving along the z -axis. The position of the LDA measurement plane is shown in Fig. 4.

The accuracy of the LDA measurement was estimated to be approximately ± 0.01 m/s, which corresponds to 0.2% of the rotor's peak-induced velocity.

2.3 PIV: apparatus, methodology and accuracy

Two component PIV in the symmetry plane along the longitudinal centre line of the rotor was performed in order to assess the structure of the flow field. A 532 nm wavelength Litron double cavity oscillator amplified, Nd:YAG laser with an output energy of 100 mJ per pulse was used to deliver the light sheet. A Phantom V341 digital high speed 4 Megapixel camera with a 2560×1600 pixel CMOS sensor fitted with a Samyang 135 mm focal length set to $f\# = 2.0$ was used to acquire the raw images. The same seeding used for LDA was also used for the PIV investigation.

The flow field produced by the shrouded rotor was split into two distinct regions: Region 1, shroud outlet, and Region 2, around the shroud, as shown in Fig. 4. A single region of interest (Region 3) was used to investigate the flow field produced by the unshrouded rotor, since this had already been investigated in detail by Green et al. (2005). Three sets of 600 image pairs were recorded at a frequency of 200 Hz for a range of counterflow velocities for each of the regions of interest investigated. A time delay of $\Delta t = 200$ μ s was used for all experimental configurations investigated.

Post-processing of the raw PIV images was completed using the commercially available software *Davis* V8.2. PIV of image regions closer than 0.004 m to the solid surface of the shroud was unreliable as a result of glare; therefore, measurements were only made to within 0.005 m of the shroud surface. The PIV velocity fields were produced using a multi-pass cross-correlation algorithm with interrogation windows of 48×48 pixels with a 50% overlap, followed by an interrogation window of 24×24 pixels with a 50% overlap. The resolution and the magnification factor (M) slightly varied among the different regions, but they can be considered to be on average $0.002R$ and 6.5 pixels/mm, respectively. The uncertainty of the PIV velocity measurements was therefore estimated to be approximately $\epsilon_u = 0.1/(M\Delta t) = 0.08$ m/s for each of the interrogation regions (Raffel et al. 2007). A maximum displacement error of 0.1 pixels was assumed for each of these PIV regions.

The unsteadiness of the flow field was assessed by calculating the root mean square (RMS) of the fluctuations of the measured axial velocity about the mean axial velocity.

Proper orthogonal decomposition (POD) by single value decomposition of the flow field was performed to identify the dominant flow structures of the flow field (F) in accordance with the method summarised by Taira et al. (2017). In POD, the flow field, which contains the individual velocity components of each instantaneous PIV image pair, is decomposed into a set of orthonormal basis functions that represent the flow field in the most 'optimal' way ($F = \Phi\Sigma\Psi$). Matrices Φ and Ψ contain the left and right singular vectors of F , and matrix Σ contains the singular values along its leading diagonal. The temporal coefficients associated with each POD mode are contained within the columns of matrix Ψ (i.e. the reconstruction coefficients of POD mode m are contained within the ' m 'th column of matrix Ψ). When referring to POD analysis, 'optimal' is used to describe the relative contribution of a given POD mode to the overall kinetic energy of the flow structures. That is, large energetic flow structures that systematically appear in the flow field are captured in the first few POD modes. As POD is based on a solution of an eigenvalue problem, the signs of the eigenvectors which constitute the POD modes are arbitrary and strongly dependent on the solution procedure. Normalisation of the singular values with respect to the sum of all other singular values allowed the probability of occurrence of that mode in the fluctuating flow to be deduced. Summation of the generated modes allows the mean flow field to be reconstructed from the POD modes. To test the statistical convergence of the POD analysis, it was performed using 300 and 600 PIV image pairs. The results obtained from processing fewer vector maps were qualitatively similar to those obtained using 600 for the first few POD modes. However, for higher POD mode numbers ($m > 6$), significant differences were observed.

3 Results

3.1 Characterisation of the flow field in hover

The flow field produced by the isolated and shrouded rotors operating in hover was characterised using LDA and PIV. Firstly, LDA allowed for the averaged induced velocity across the shroud outlet to be estimated. The hover-induced velocity U_i is typically used to scale the descent velocity U_o of the rotor, $\alpha = (|U_o|/U_i)$. Subsequently, further LDA and PIV investigations disclosed the main average and unsteady features of the flow produced by the shrouded and unshrouded rotors.

3.1.1 Analysis of the mean flow in hover

The mean axial velocity component (u) measured by means of LDA in a cross-stream plane $1.48R$ upstream (with respect to the wind tunnel flow direction) of the rotor disc is presented in Fig. 5 for the shrouded rotor case. It was not possible to characterise the induced velocity inside the shroud due to optical access; therefore, measurements of the wake were taken on the aforementioned plane. Based on the axial velocity profile generated by the shrouded rotor, the notional induced velocity $U_i = 3.3 \text{ m/s}$ was calculated using equation 1, where u is the time-averaged induced velocity of the rotor, and A_i is the area of the region investigated using LDA.

$$U_i = \frac{\int_0^{1.1R} \int_0^{2\pi} u r dr d\theta}{A_i} \quad (1)$$

The notional induced velocity of the shrouded rotor was used to scale the descent velocity of both the isolated and the shrouded rotor ($\alpha = |U_o|/U_i$). Moreover, U_i can also be used to roughly estimate the thrust coefficient of the rotor using momentum theory as follows:

$$c_T = \frac{T}{\rho A V_{tip}^2} = 2 \left(\frac{V_{ind}}{V_{tip}} \right)^2 = 4 \cdot 10^{-3}, \quad (2)$$

where T is the rotor thrust, ρ is the air density, A is the rotor disc area and $V_{ind} = U_i/2$, since U_i was measured at a

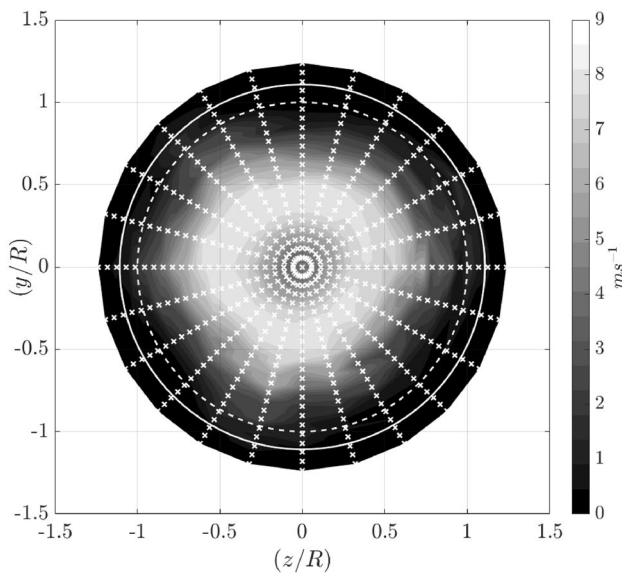


Fig. 5 Averaged axial velocity component (u) produced by the shrouded rotor operating in hover $0.48R$ from the shroud outlet plane ($x/R = 0.48$). This figure was produced using LDA and each sample point location is displayed by a white cross. The rotor blade tip path dashed line (white) and the shroud outlet lip solid line (white) have been projected onto the plane of investigation

distance from the rotor where the wake is fully developed and the average induced velocity is roughly twice that on the rotor disc.

LDA velocity profiles along the vertical (y) and horizontal (z) axes of both the unshrouded and shrouded rotor outlet planes are presented in Fig. 6. Axial, radial (along the y -axis) and tangential (along the z -axis) velocity distribution are presented in Fig. 6A, B and C, respectively. Blockage effects resulting from the shroud support struts on the inlet side of the rotor are believed to be responsible for the slight variation of axial velocity profiles between the two sweep directions. The extracted profiles presented in Fig. 6 indicate that the shroud does not significantly affect the mean axial velocity profile produced by the rotor, apart from the region $|r/R| \leq 0.2$, where the mounting of the shroud on the motor cowling produces a slightly lower velocity. The expected increase in the axial induced velocity due to the shroud-enhanced thrust is not overly evident, probably caused by the distance of the investigation plane from the rotor due to the presence of the shroud. By comparing the radial and tangential velocity profiles produced by the shrouded rotor and the unshrouded rotor on a plane ($x = 1.48R$) from the rotor disc plane, it is clear that the effect of the shroud on the mean outflow is negligible. It is postulated that this is a consequence of this particular shroud design.

The mean flow fields, measured using PIV, produced by the unshrouded and shrouded rotors are presented in Fig. 7A and B, respectively. It should be noted that Fig. 7B is produced by stitching together the mean flow field results of two PIV regions of interest using linear interpolation. Comparison of these two figures shows that the wake produced by the shrouded rotor is topologically similar to that produced by the isolated rotor, with a region of low velocity air surrounded by a ring of high velocity air. Appreciable differences between the two cases can be observed in how the air is entrained in the rotor inflow as a result of the shroud, which forces the streamlines to curve in a more prominent way before entering the rotor disc. Past investigations into the flow field produced by a shrouded rotor, performed by Martin and Tung (2004), identified a region of reverse flow underneath the rotor's centre body. This region of reverse flow is not observed in the mean flow field presented in Fig. 7B or the LDA velocity profiles presented in Fig. 6. The absence of a rotor centre body inside of the shroud is believed to be responsible for this variation of the mean velocity profile.

3.1.2 Unsteadiness of the flow in hover

The RMS of the axial velocity component (u_{rms}) produced by the shrouded rotor is presented in Fig. 8. The wake from a shrouded rotor shows four distinct regions of unsteadiness, which broaden and merge together as the distance from the

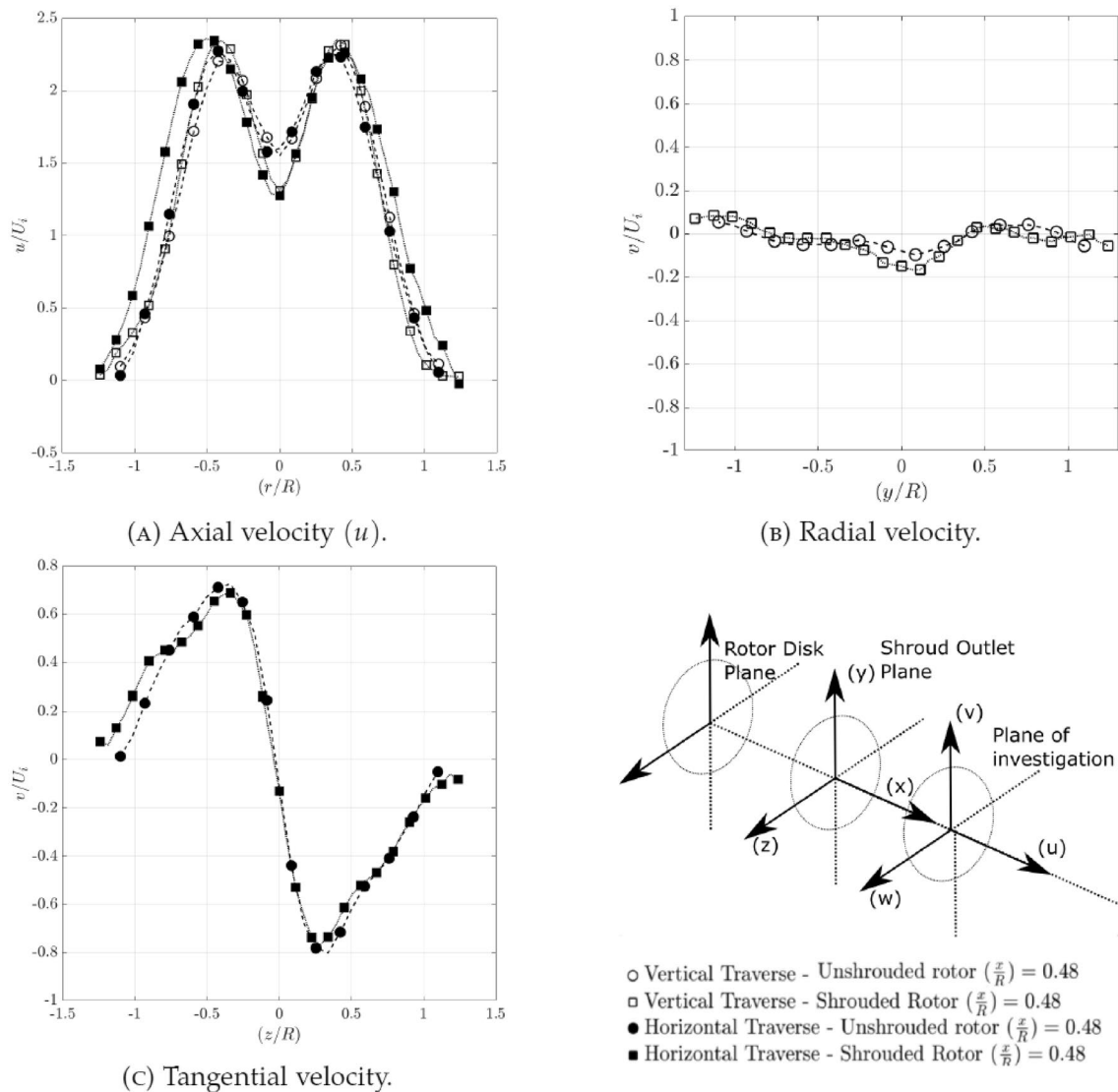


Fig. 6 LDA velocity profiles along the horizontal and vertical axes of symmetry of the shrouded and unshrouded rotor measured at $1.48R$ from the rotor disc plane ($x/R = 0.48$)

shroud outlet plane is increased. This unsteadiness is associated with the shear layers produced by the shrouded rotor’s wake interacting with the quiescent surroundings and the inner low-velocity core of the wake itself. The maximum RMS of the velocity fluctuations (about 50% of U_i) can be observed in the wake slipstream region. The RMS velocity distribution for the isolated rotor, not reported here for the sake of brevity, was substantially similar to the one for the shrouded rotor, but with a slightly higher peak unsteadiness of the order of 60% of U_i .

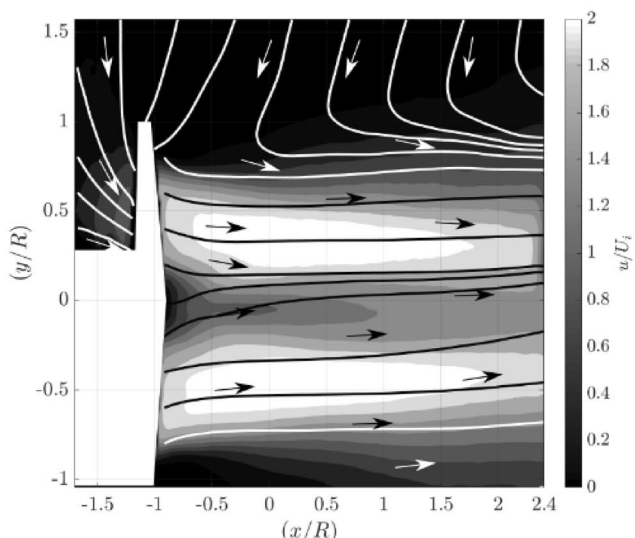
3.2 Characterisation of the flow field in axial descent

The flow field produced by the isolated and shrouded rotors operating in axial descent was then characterised using LDA

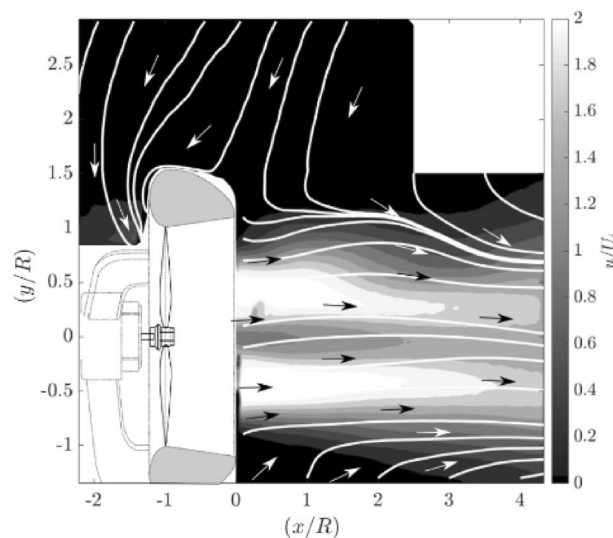
and PIV. The wind tunnel speed was set to reproduce descent velocity ratios $\alpha = (|U_o|/U_i)$ ranging from 0 to 2. Firstly, time-averaged LDA velocity profiles and PIV flow fields were analysed to assess the differences in the development of the mean flow field for both rotors, and then, RMS of velocity fluctuations and POD analysis provided insight into the unsteady features of the flow and its dominant structures.

3.2.1 Analysis of the mean flow in axial descent

Figures 9 and 10 show the development of the LDA mean velocity profiles produced by an isolated and a shrouded rotor on a plane $1.48R$ from the rotor disc plane, $x/R = 0.48$, as the velocity ratio was increased from $\alpha = 0$ to $\alpha = 2.0$.



(A) Isolated rotor.



(B) Shrouded rotor.

Fig. 7 Mean axial velocity profile (u) produced by the unshrouded (A, PIV region 3) and shrouded rotor (B, PIV Region 1 and 2 combined) operating in hover. The velocity has been scaled with respect to the notional induced velocity (U_i) at the shrouds outlet. Mean flow

streamlines have been indicated to highlight specific features of the flow field. Note that for the shrouded rotor case the mean velocity profile of PIV region 1 and 2 was stitched together using linear interpolation

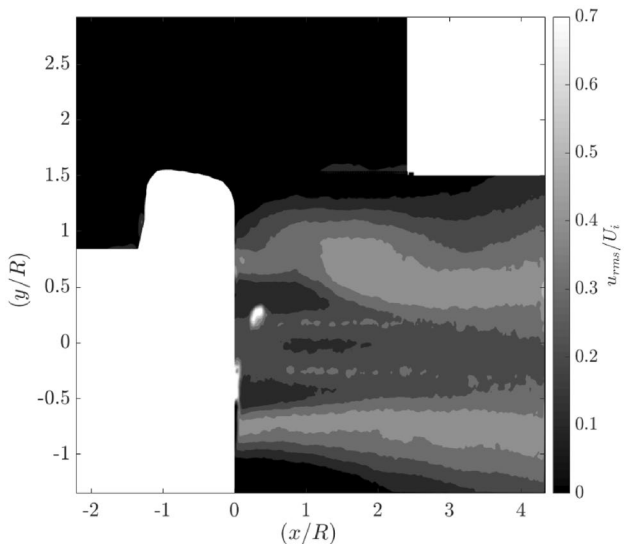


Fig. 8 Contour plots of the RMS of the fluctuations about the mean axial velocity (u_{rms}) produced by the shrouded rotor operating in hover. The RMS of the fluctuations is scaled with respect to the notional induced velocity of the shrouded rotor (U_i). Note this is a montage of the RMS of the fluctuations about the mean axial velocity profiles of PIV regions 1 and 2 stitched together using linear interpolation

Let us first focus on the isolated rotor case. When increasing the wind tunnel speed up to a velocity ratio of $\alpha = 1.2$, the mean axial velocity profile developed to resemble that of a round jet, with a single peak velocity

located at the centre of the rotor ($y/R = 0$) (Bernero 2000). The two separate velocity peaks associated with hovering rotors at a radial ordinate of $y/R = \pm 0.7$ could no longer be observed in this particular plane of investigation. This is coupled with the gradual change of direction of the radial velocity component, shown in Fig. 9B, that starts negative at low α for the upper part of the rotor due to the contraction of the wake, and then become strongly positive, indicating that the rotor wake is deflected radially outboard. At the plane of investigation, the peak radial velocity occurs at $\alpha = 1.2$ outboard of the rotor at radial ordinates of $y/R = \pm 1.4$. At higher velocity ratios ($\alpha \geq 1.3$) the axial velocity profile becomes negative ($u < 0$) indicating that the interaction between the rotor wake and the wind-tunnel free stream occurs downstream of the plane of investigation, accompanied by a reduction in the magnitude of the radial component. At $\alpha = 1.3$, a region of higher magnitude axial velocity flow forms in the centre of the rotor, surrounded by a region of lower velocity flow (Fig. 9A). This indicates that the wind-tunnel free stream penetrates through the plane of investigation in line with the rotor hub. As α is further increased, the velocity profile becomes flatter and tends to the free-stream velocity value. Analysis of Fig. 9C shows that the tangential velocity of the rotor wake gradually reduced from a maximum at $\alpha = 0.0$, to zero at a velocity ratio of $\alpha = 1.4$. At descent velocity ratios $\alpha \geq 1.4$ the wind-tunnel free stream penetrates through the plane of investigation, and the rotors swirl no longer propagates in the positive x -direction.

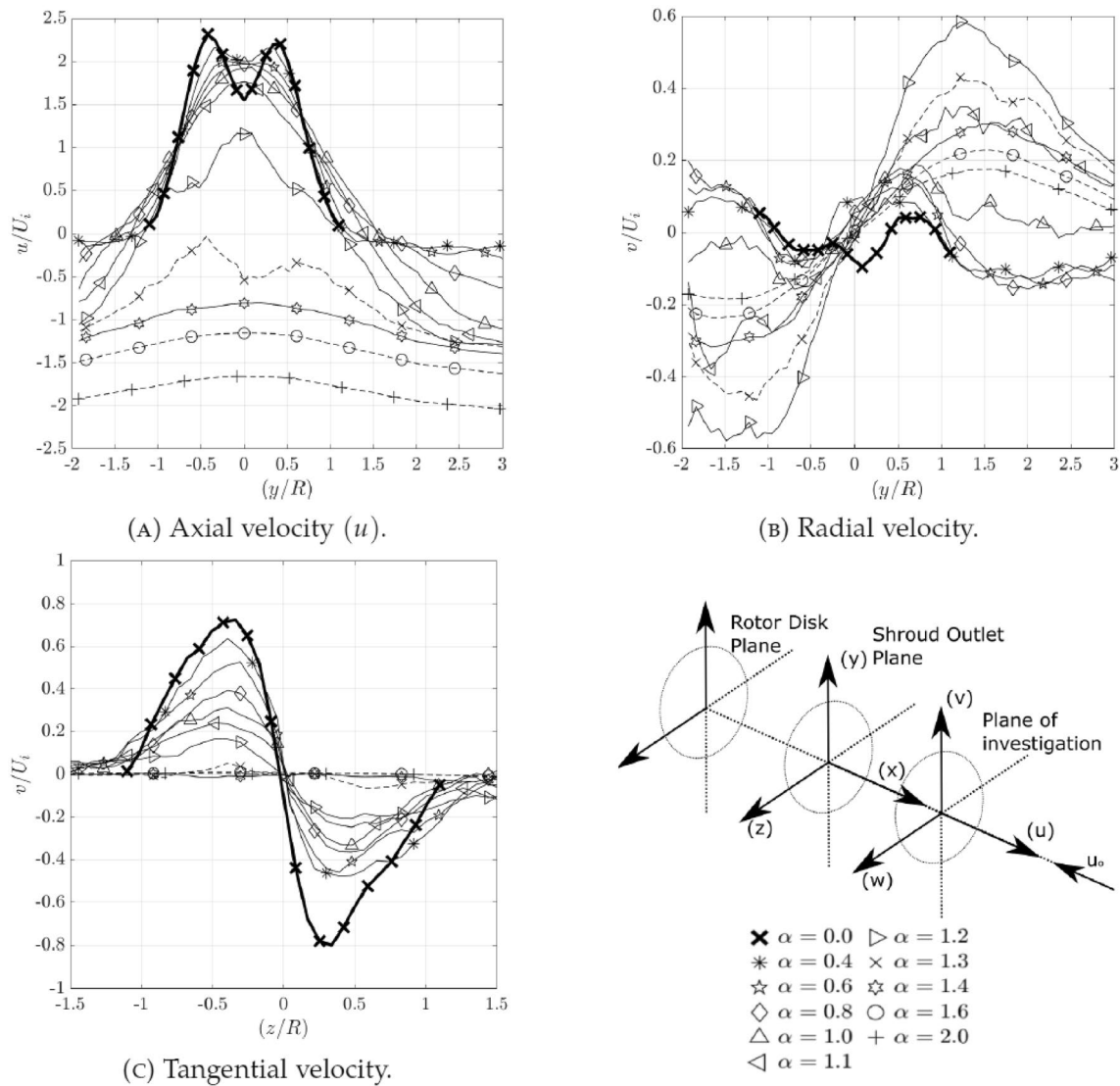


Fig. 9 LDA mean velocity profiles along the vertical axis of symmetry of the isolated rotor on a plane $1.48R$ from the rotor disc plane ($x/R = 0.48$), as the descent velocity ratio was varied from $\alpha = 0$ to $\alpha = 2.0$

For the shrouded rotor (see Fig. 10), similar trends with respect to the isolated rotor were observed. It is clear that, at velocity ratios below ($\alpha = 1.2$), the velocity profile produced by the shrouded rotor is similar to that produced by the unshrouded rotor on this plane of investigation. As the velocity ratio was increased from $\alpha = 0.4$ to $\alpha = 0.9$, the mean axial velocity profile becomes uniform across a large portion of the shroud outlet plane ($|y/R| \leq 0.4$). No significant effect could be observed in the mean axial velocity profile across the shroud outlet plane ($|y/R| \leq 1.0$), when the descent velocity ratio was increased from $\alpha = 0.4$ to $\alpha = 1.2$. More significant changes in behaviour between the two configurations were observed for $\alpha \geq 1.2$. For a better comparison in this range of descent velocity ratios, the axial velocity profiles for the shrouded and unshrouded rotors are presented

together in Fig. 11. Starting from $\alpha = 1.2$ the profiles of the unshrouded rotor flatten at a faster rate than those of the shrouded rotor, suggesting that the shroud might slightly delay the onset of the VRS. A further increase in the descent velocity leads to more homogeneous velocity profiles that eventually collapse onto the free-stream velocity. Significant differences between the two configurations can be observed in the behaviour of the radial velocity, Figs. 10B and 9B. At low α values the radial velocity component of the wake once again starts negative for the upper part of the rotor due to the contraction of the wake. However, at higher descent velocity ratios, the shroud prevents the gradual increase in the radial velocity component leading to a sudden increase in the radial velocity component of the wake. This occurs as a result of the deflection of the shrouded rotor wake and

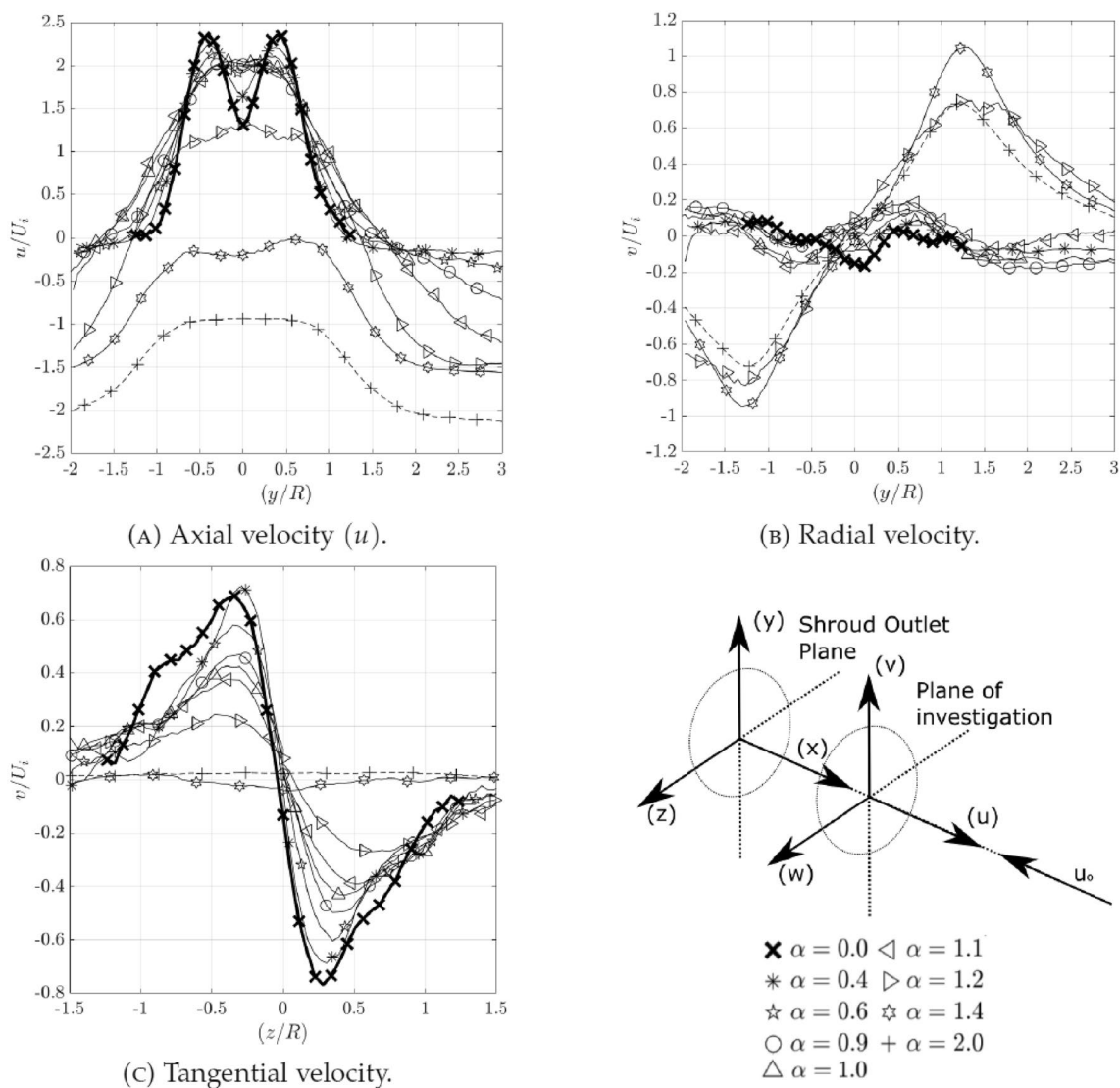


Fig. 10 LDA mean velocity profiles along the vertical axis of symmetry of the shrouded rotor on a plane $1.48R$ from the rotor disc plane ($x/R = 0.48$), as the descent velocity ratio was varied from $\alpha = 0$ to $\alpha = 2.0$

the wind-tunnel free stream around the shroud. Analysis of Fig. 10C shows that the tangential velocity profile of the shrouded rotor, operating in axial descent, is similar to that produced by the unshrouded rotor on the same plane of investigation. Both show the gradual reduction of the tangential velocity component to zero at $\alpha = 2.0$.

Figures 12 and 13 show the development of the mean flow fields measured by means of PIV, upstream of the isolated and shrouded rotor, as the descent velocity was increased from hover $\alpha = 0$ to $\alpha = 1.4$. Mean flow streamlines, calculated using a forward Euler prediction algorithm, were used to highlight specific features of the flow field. As expected, the results presented in Fig. 12 related to the mean flow field produced by an isolated rotor operating in axial descent were similar to those presented by Green et al. (2005). These

results showed that, at low descent velocity, the near flow field is similar to that produced by a hovering rotor. As the descent velocity increased, the rotor wake was increasingly encroached upon by the wind-tunnel free stream. At the interaction between the rotor wake and the wind-tunnel free stream, a stagnation point forms in line with the rotor hub. Analysis of Fig. 12B, C and D shows that the stagnation point moves towards the rotor disc plane as the descent velocity increases. It is hypothesised that, at low descent velocities, the interaction between the rotor wake and the wind-tunnel free stream will occur outside of the region of investigation ($x/R > 2.0$). At higher descent velocity ratios a conical region of reverse flow penetrates up to the rotor disc plane. Outboard of the rotor a large region of recirculation forms. At a velocity ratio of $\alpha = 1.0$ the centre of the

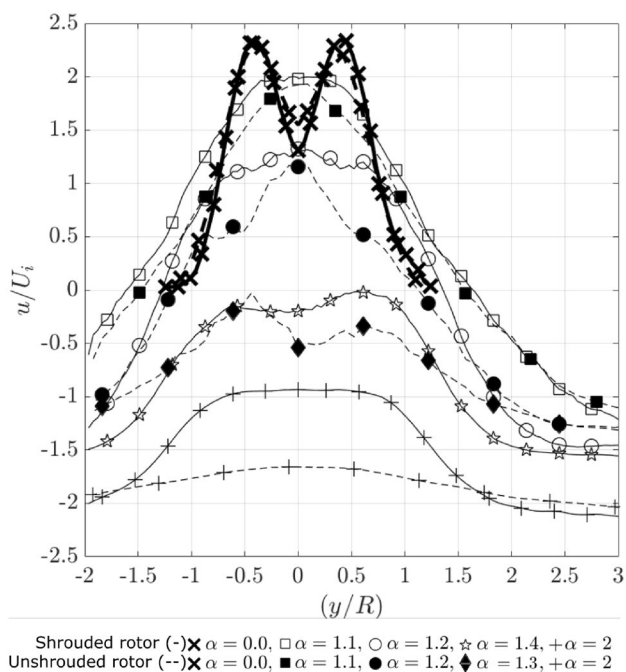


Fig. 11 Selective comparison of the mean LDA velocity profiles along the vertical axis of symmetry of the shrouded and unshrouded rotor, on a plane $1.48R$ from the rotor disc plane ($x/R = 0.48$), as the descent velocity was varied from $\alpha = 0$ to $\alpha = 2.0$

recirculation is located $1.2R$ from the rotor disc plane and $1.2R$ outboard of the rotor hub ($x/R = -0.3, y/R = 1.2$). As the descent velocity was increased, the recirculation moves from below the rotor to above the rotor disc plane until the rotor enters the windmill brake state. The flow topology described above is characteristic of the flow field produced by a rotor operating in the VRS.

Figure 13 shows the development of the mean flow field produced by the shrouded rotor for the same range of descent velocity ratios. When compared to the PIV measurements of an isolated rotor the same general topological features can be observed. At low descent velocities, the flow field resembles that of a round jet, with a single centralised velocity peak located on the geometric centreline of the shroud. The ring of high velocity air surrounding a region of low velocity air can no longer be observed. Mean flow stagnation points form at the interface between the rotor wake and the wind-tunnel free stream, on the geometric centreline of the shroud as a result of the radial deflection of the rotor wake. Analysis of Fig. 13 shows again that the stagnation point moves towards the shroud outlet plane as the descent velocity was increased.

Figure 14 presents a more quantitative analysis of the mean stagnation point locations produced by both configurations for the range of α values investigated. The mean

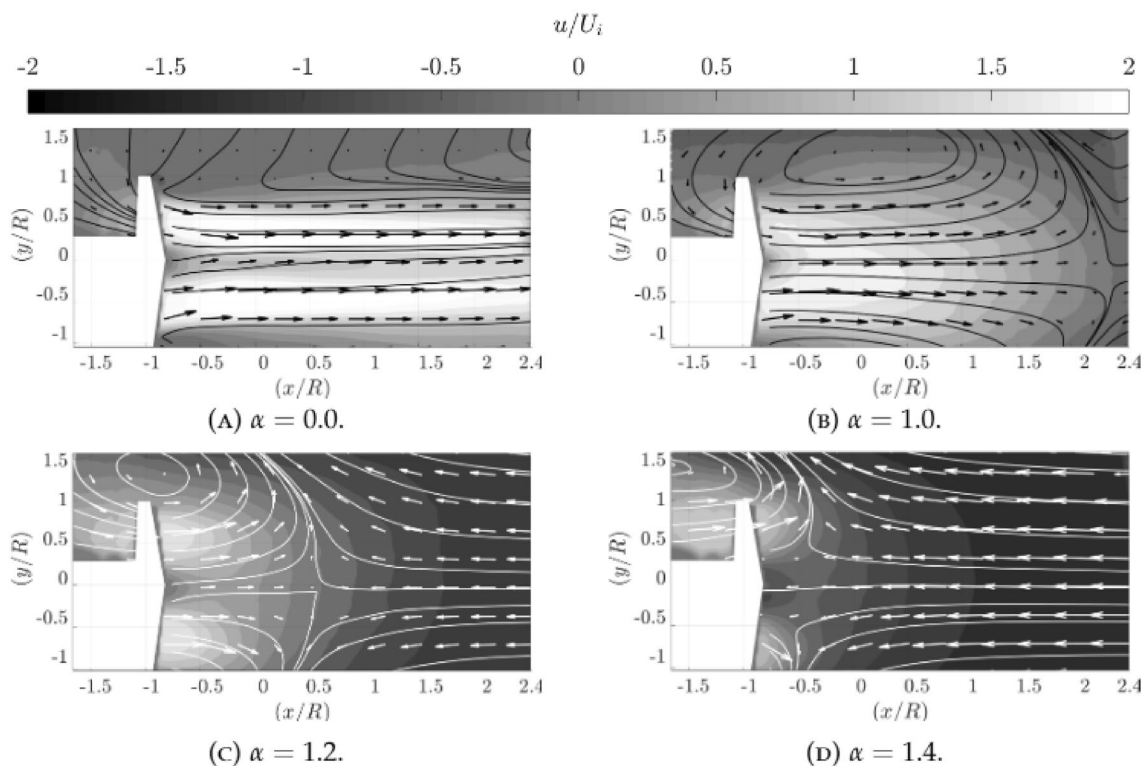


Fig. 12 Averaged mean axial velocity contour plots of the unshrouded rotor (PIV: Region 3) as the descent velocity $|U_o|$ increases from $\alpha = 0.0$ to 1.4 . Velocity is scaled with respect to the

notional induced velocity U_i . Streamlines and a reduced number of velocity vectors are superimposed onto the contour plots

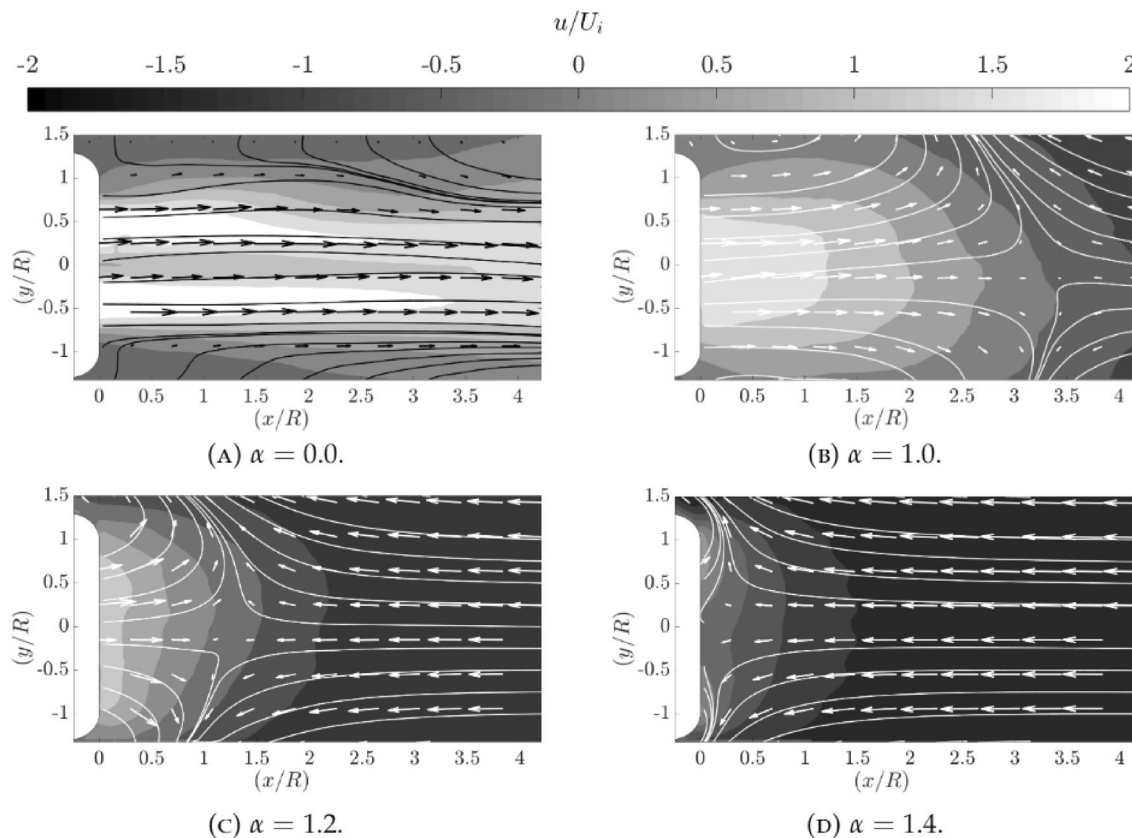


Fig. 13 Averaged mean axial velocity plots of the shrouded rotor (PIV: Region 1) as the descent velocity $|U_o|$ increases from $\alpha = 0.0$ to 1.4. Velocity is scaled with respect to the notional induced velocity

U_i . Streamlines and a reduced number of velocity vectors are superimposed onto the contour plots

location of the stagnation point was extracted from the centreline axial velocity profiles at $y/R = 0$ in the test conditions where it fell inside the PIV investigation window. Analysis of Fig. 14 shows that stagnation points produced by both the shrouded and unshrouded rotor wake’s interaction with the free stream flow move towards the shroud outlet plane, or the rotor disc plane as the descent velocity was increased. In particular, at every descent velocity, the stagnation point appears to be closer to the rotor disc plane for the unshrouded configuration when compared to the shrouded one. This suggests that the overall development of the VRS is slightly delayed by the presence of the shroud, as previously inferred from the LDA data presented in Fig. 11.

The development of the mean flow field around the shroud (Region 2) is shown in Fig. 15. At low descent velocities, the mean flow field produced by the shrouded rotor is similar to that produced by the isolated rotor. At $\alpha = 0.8$ the centre of the recirculation, shown in Fig. 15B, is located approximately $2.4R$ upstream of the shroud outlet plane and $2.0R$ from the core of the shroud. As the descent velocity increased, the recirculation moved from upstream of the shroud to around the side of the shroud, as shown in

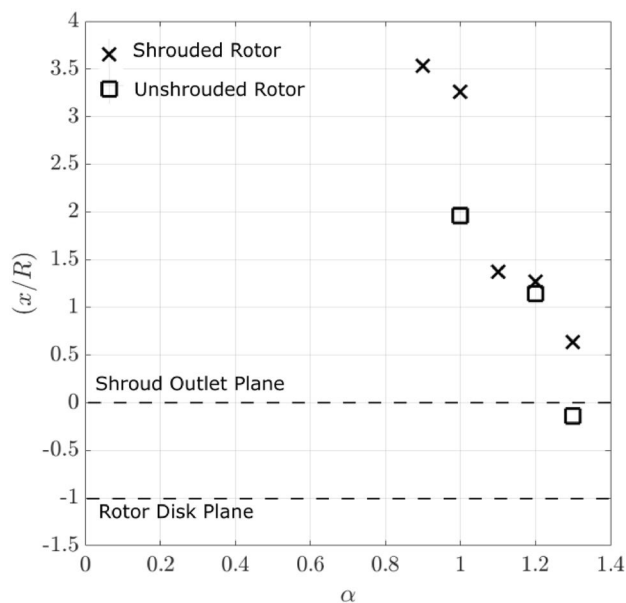


Fig. 14 Mean location of the stagnation point obtained from PIV measurements of the flow field produced by the unshrouded and the shrouded rotor in axial descent

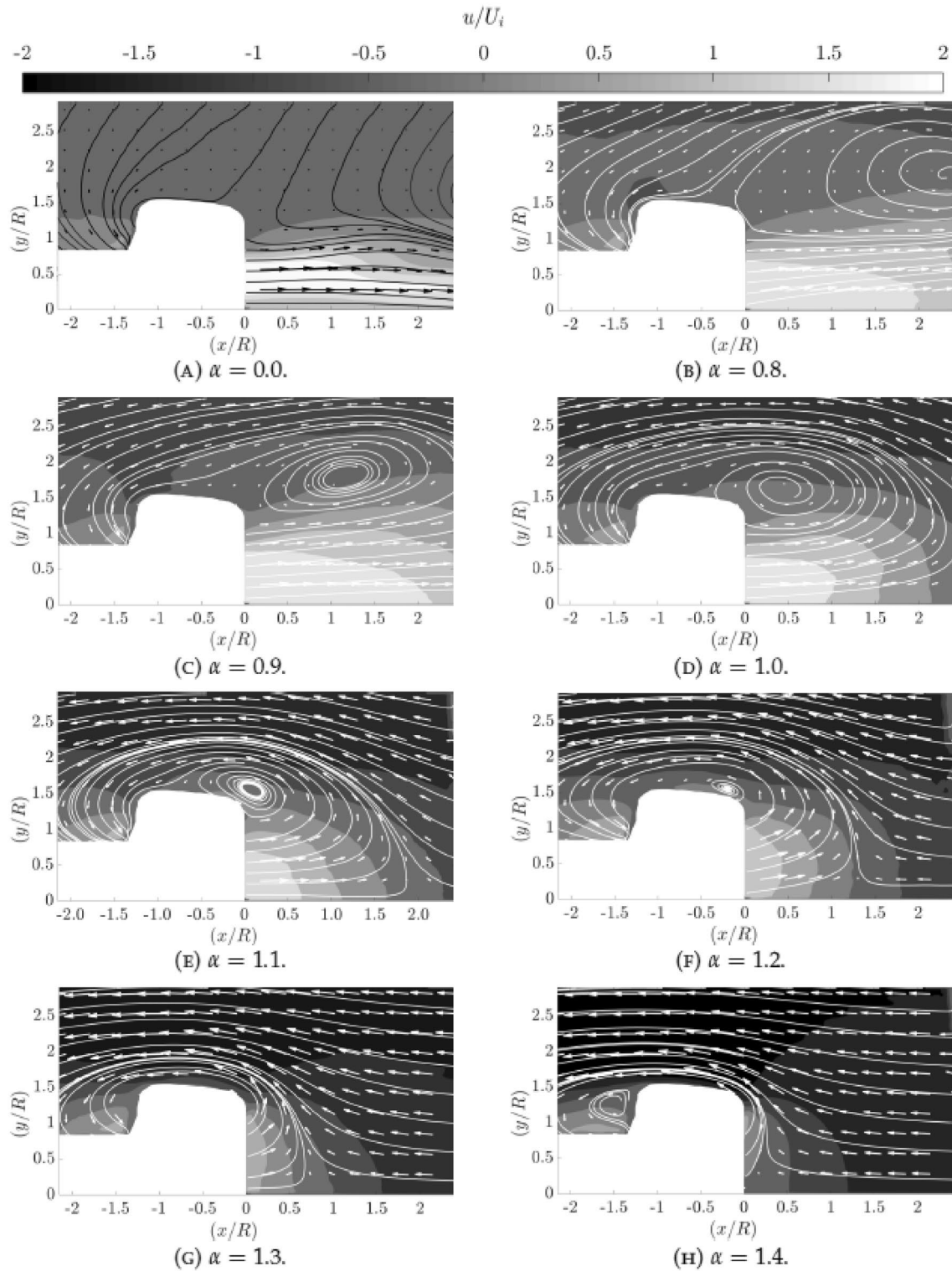


Fig. 15 Averaged mean axial velocity plots of the shrouded rotor (PIV: Region 2) as the descent velocity $|U_o|$ increases from $\alpha = 0.0$ to 1.4. Velocity is scaled with respect to the notional induced velocity

U_i . Streamlines and a reduced number of velocity vectors are superimposed onto the contour plots

Fig. 15E, where at $\alpha = 1.1$, the centre of the recirculation is located close to leading edge of the shroud outlet ($x/R \approx 0$, $y/R \approx 1.5$). At higher values of α , the centre of the recirculation is no longer visible. In particular, for $\alpha = 1.4$, a secondary recirculation region can be observed downstream of shroud inlet plane inside of the larger recirculation region.

Figure 16 shows the mean flow field produced by both rotors when they are operating at a descent velocity ratio of $\alpha = 2.0$. At this velocity ratio, no air exits the shroud through the shroud outlet plane. Instead, the wind-tunnel free stream passes through and around the shroud. At this point, both rotors are operating in a state analogous to the windmill brake state.

3.2.2 Unsteadiness of the flow in axial descent

Figures 17 and 18 show contour plots of the RMS of the axial velocity fluctuations about the local mean axial velocity for the isolated and shrouded rotor, respectively. The RMS of the fluctuations is scaled with respect to the notional induced velocity of the shrouded rotor (U_i).

Figure 17B shows that at a velocity ratio of $\alpha = 1.0$, a crescent-shaped region of high RMS of the axial velocity fluctuations forms on the rotor centreline approximately $2.5R$ from the rotor disc plane. The location of this unsteadiness coincides with the location of the stagnation point identified earlier in Fig. 12B. As the velocity ratio increases from $\alpha = 1.0$ to $\alpha = 1.2$, the location of unsteadiness moves with the stagnation point. The maximum RMS is obtained for this α value, about 90% of the notional induced velocity. As alpha is increased, the disappearance of the stagnation

point from the field of view means that the flow field returns to a form where the unsteadiness is dominated by the wake produced by the blade tip vortices, as they propagate around the rotor disc. The extent to which the unsteadiness propagates upstream away from the rotor disc plane decreases as α increases.

The unsteadiness of the flow field produced by the shrouded rotor operating in axial descent (Fig. 18) is similar to that produced by the isolated rotor once mirrored with respect to the rotor rotation axis. At moderate velocity ratios, see Fig. 18B, the ring of high unsteadiness associated with the shear layer of the wake broadens, diffusing laterally as the wake propagates away from the shroud. With respect to the hovering case, the interaction between the rotor wake and the wind-tunnel free stream leads to an increase in the RMS of the axial velocity fluctuations over the entire field of view and around the shroud, i.e. the wind-tunnel free stream transports turbulent air back into the field of view. As with the isolated rotor, at higher velocity ratios, a region of unsteadiness forms at the location of the stagnation point. The magnitude of this unsteadiness is similar to that produced by the isolated rotor ($u_{rms} \approx 0.9U_i$). Once again, the region of unsteadiness approached the shroud outlet plane as the descent velocity increased. The formation of this region of unsteadiness is coupled with an increase in the unsteadiness of the flow field outboard of the shroud. It is clear from the analysis of the mean flow field, see Fig. 15C, that the large recirculation which forms outboard of the rotor is responsible for the high RMS values observed in Fig. 18C. Once the stagnation point can no longer be observed in the field of view, the unsteadiness of the flow field, as for the isolated

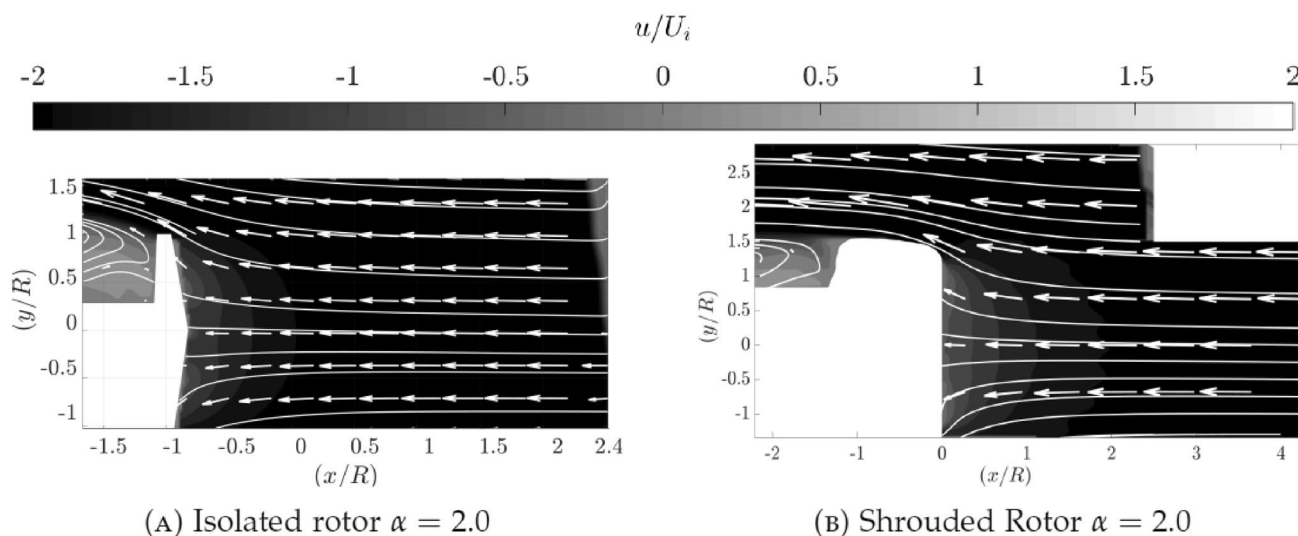


Fig. 16 Mean axial velocity plots of flow field produced by the unshrouded (A, Region 3) and shrouded rotor (B, Region 1 and 2 combined) operating at a descent velocity ratio of $\alpha = 2.0$. Velocity

is scaled with respect to the notional induced velocity U_i . Streamlines and a reduced number of velocity vectors are superimposed onto the contour plots

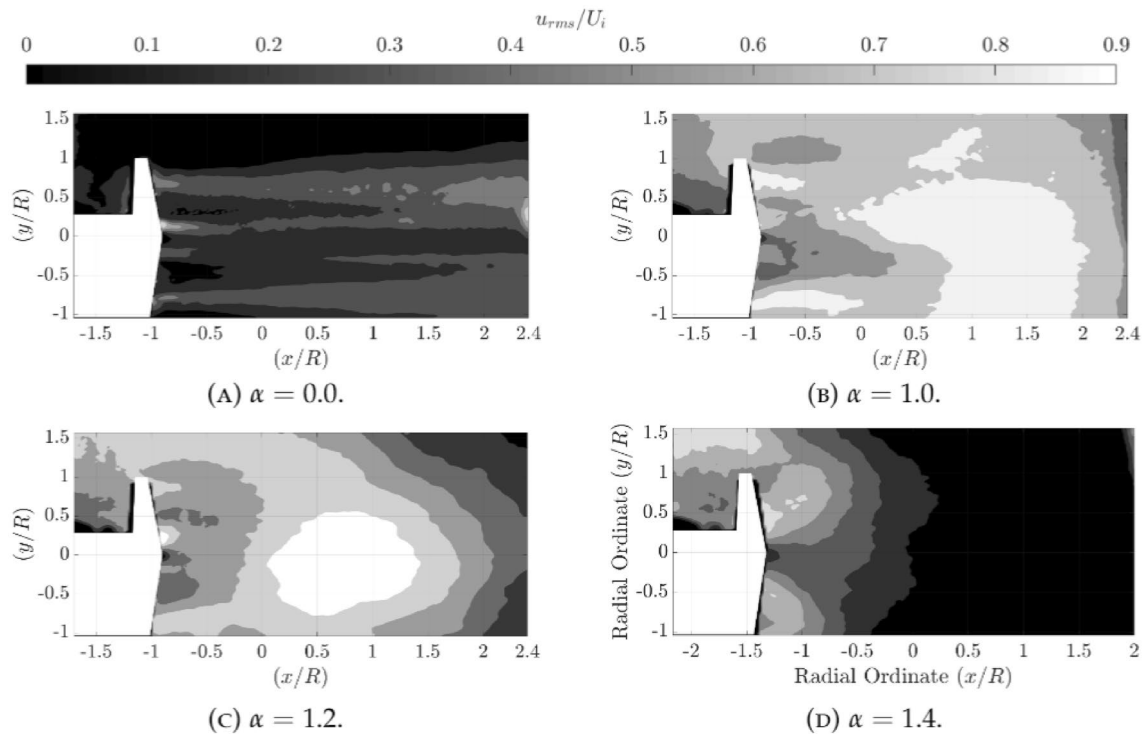


Fig. 17 RMS of the axial velocity components of the flow field produced by the unshrouded rotor (PIV Region 3) as the descent velocity ratio increases from $\alpha = 0.0$ to 1.4. The RMS of the fluctuations is scaled with respect to the notional induced velocity (U_i)

rotor, becomes dominated by the rotor wake as it propagates around the side of the shroud. At a velocity ratio of $\alpha > 1.1$, a region of significant unsteadiness forms at the lip of the shroud outlet, in correspondence to where the centre of the recirculation regions has moved.

3.2.3 POD analysis

Visualisations of the first four eigenmodes produced by applying snapshot POD to the PIV results of the unshrouded rotor (PIV Region 3) and the shrouded rotor (PIV Region 1) in hover ($\alpha = 0$) are presented in Figs. 19 and 20, respectively. The first two POD modes of the isolated rotor used in this investigation, shown in Fig. 19A and B, indicate that the most probable and energetic representations of the flow field are dominated by the blade root vortices. The unsteadiness associated with the passage of the blade tip vortices and the passage of the vortex sheet trailed from behind the rotor blades was observed starting from mode 4. Spectral analysis of the reconstruction coefficients showed that both of these POD modes had a dominant frequency equal to the rotational frequency of the rotor (66Hz).

The first four eigenmodes of the flow field produced by the shrouded rotor shown in Fig. 20 differ considerably from those of the hovering isolated rotor, shown in Fig. 19. The first three modes shown in Fig. 20A–C are associated

with radial flapping across the diameter of the shroud outlet. In particular, the first mode is more relevant in a region approximately one diameter from the shroud outlet, whereas modes 2 and 3 are associated with the shear layer produced by the shroud lip. Mode 4 appears to be associated with the root and tip vortices that have broken down by the time they exit the shroud. This was confirmed by the analysis of the instantaneous vorticity data computed from the PIV data, that didn't show any clear vortical structure for the shrouded rotor case (in contrast to the unshrouded case).

It should be noted that for the $\alpha = 0$ cases, both the shrouded and unshrouded rotors show a slow convergence of the progressive sum of the modal energies with respect to the moderate wind-on test cases. This indicates that the unsteadiness is more evenly distributed between the modes and the single contribution of the first modes is limited.

The first two modes for the unshrouded and shrouded rotor close to VRS regime are presented in Figs. 21 and 22, respectively. The influence of each mode on the velocity field was evaluated by subtracting the reconstructed mode from the averaged flow field, as described by Patter-Rouland et al. (2001). The reconstructed modes were produced using both the maximum and minimum reconstruction coefficients of the m -th mode $\Psi(m)$. The reconstructed flow fields formed as a result of the first POD mode of the unshrouded rotor operating at a descent velocity ratio of

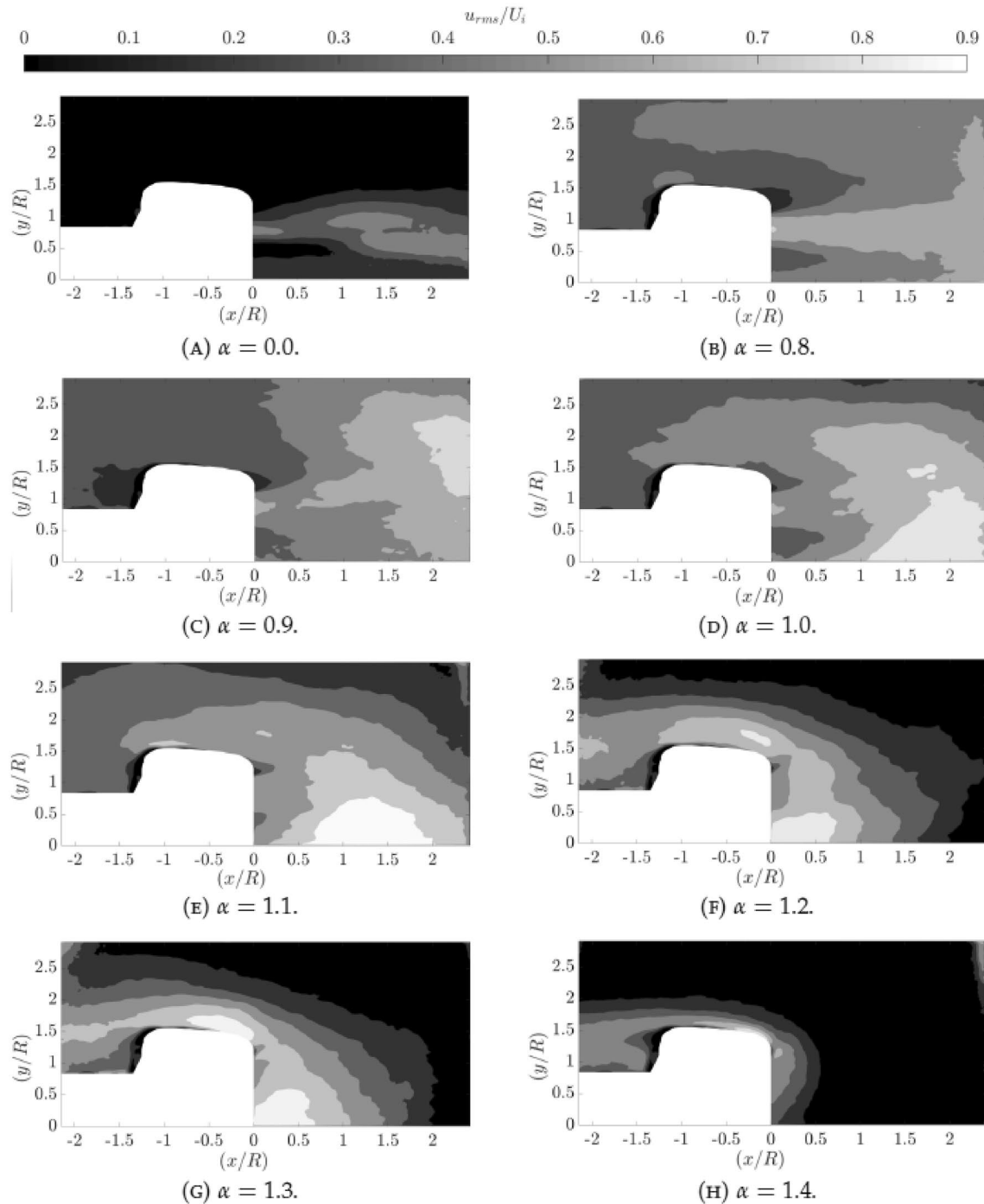


Fig. 18 RMS of the axial velocity components contour plots of the shrouded rotor (PIV: Region 2) as the descent velocity (U_o) increases from $\alpha = 0.0$ to 1.4. The velocity is scaled with respect to the notional induced velocity (U_i)

$\alpha = 1.0$, presented in Fig. 21C and E, show that the first POD mode is responsible for the variation of the penetration of the counterflow towards the rotor disc plane. Analysis of Fig. 21B shows that the unsteadiness associated with the passage of the blade tip vortices and the recirculation which forms around the side of the rotor blade tips are

contained within higher POD modes. This is expected as it was previously shown by Green et al. (2005), at moderate velocity ratios the flow field enters an incipient flow regime, where the flow intermittently switches between the topology associated with a hovering rotor and the toroidal form associated with the VRS.

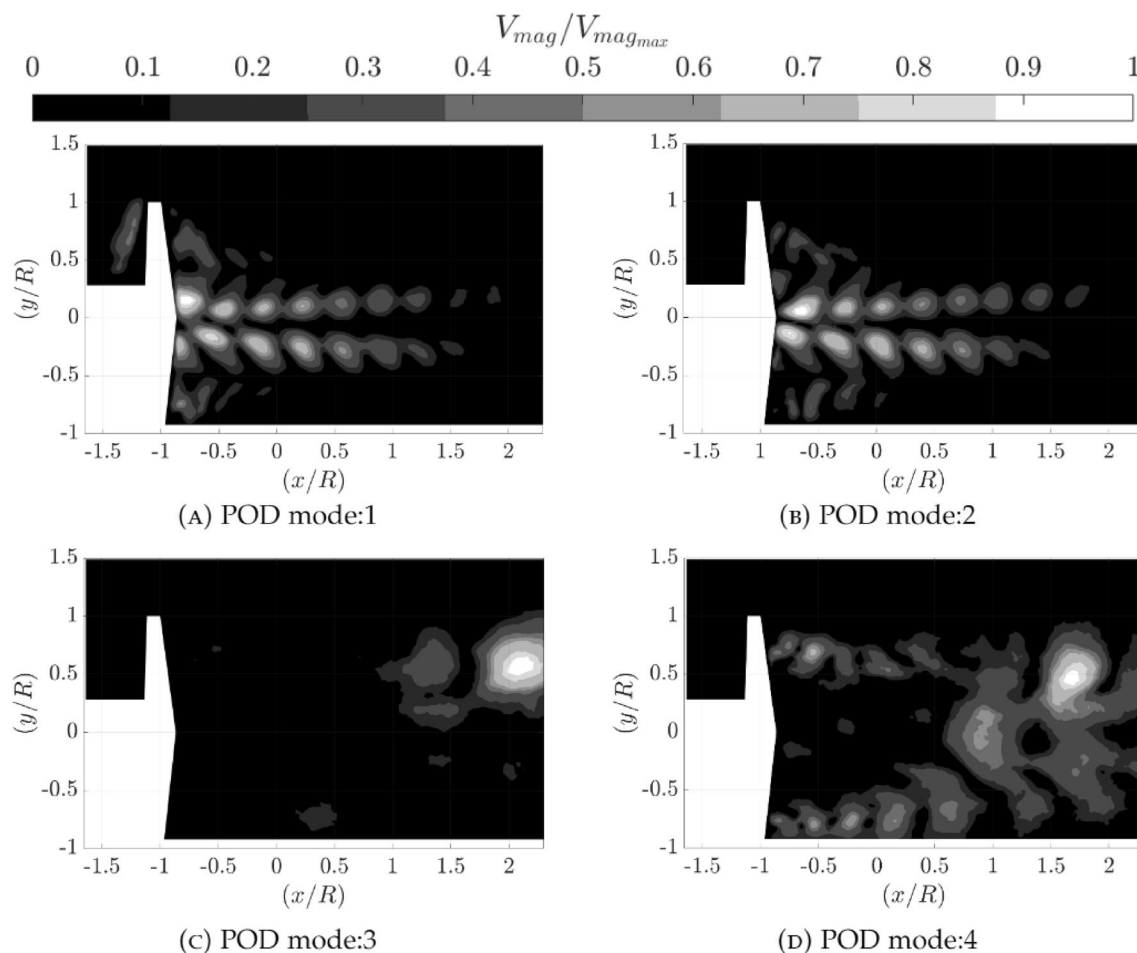


Fig. 19 Visualisation of the first four POD eigenmodes of the velocity fluctuations produced by a hovering unshrouded rotor ($\alpha = 0.0$). The modes were calculated from a sequence of 600 instantaneous

velocity fields. The vector lengths are scaled with respect to the maximum vector length of each individual mode

POD analysis of the flow field produced by the shrouded rotor operating in axial descent, shown in Fig. 22, provides insight into the underlying structure of the flow field. At low velocity ratios ($\alpha < 0.8$), not shown here for the sake of brevity, the first two POD eigenmodes are similar to those produced by a hovering shrouded rotor described earlier. At a velocity ratio of $\alpha = 1.1$, the first POD mode has one global maximum in the region directly upstream of the rotor, (Fig. 22A), whereas the second mode has two maxima in line with the lip of the shroud (Fig. 22B). Reconstructed flow fields, produced by subtracting the maximum and minimum reconstruction coefficient forms of the POD modes, are presented in Fig. 22 and show that the first mode materialises as the penetration of the wind-tunnel free stream towards the shroud outlet plane. The location of these fluctuations coincides with the region of high RMS of the axial velocity fluctuations visible in Fig. 18E. The location of the stagnation point, identified in Fig. 13, varied as a result of the flow fluctuations. The second POD mode is responsible for the

radial movement of air across the shroud outlet plane; however, it should be noted that the magnitude of these radial fluctuations is small, as the flow is no longer dominated by the axially induced velocity produced by the rotor. Radial flapping of the shrouded rotor wake can still be observed in higher POD modes, not shown here.

The progressive sum of singular values as a percentage of the total sum over a range of descent velocity ratios is shown in Fig. 23, very similar trends were observed for the hover and the isolated rotor cases. It can be noticed that the $\alpha = 2$ case shows a much slower convergence with respect to the other cases, which is expected since the flow, as shown in Fig. 16, is dominated by the homogeneous free-stream in the region of interest. This characteristically contains a larger percentage of small-scale turbulent structures, when compared to the slower descent velocity ratios investigated, which contain large-scale unsteady flow structures such as large regions of recirculation and unsteady wakes. The $\alpha = 0$ case presents the second slowest convergence, as previously

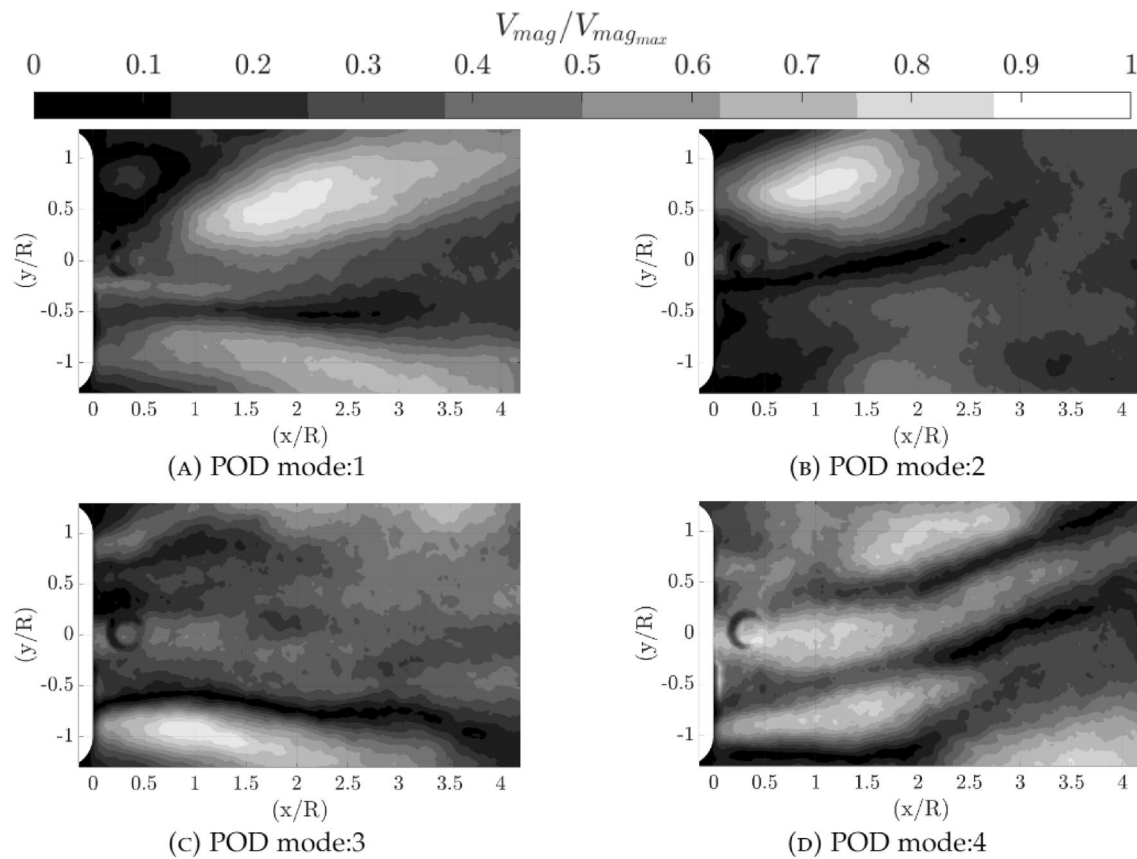


Fig. 20 Visualisation of the first four POD eigenmodes of the velocity fluctuations produced by a hovering shrouded rotor ($\alpha = 0.0$). The modes were calculated from a sequence of 600 instantaneous veloc-

ity fields. The vector lengths are scaled with respect to the maximum vector length of each individual mode

discussed when describing the POD modes of the hovering cases.

4 Conclusions

An investigation into the structure of the flow field produced by a shrouded rotor operating in hover and axial descent has been performed using Particle image velocimetry (PIV) and laser Doppler anemometry (LDA). Results were compared with those of an isolated rotor operating under the same condition to assess the effect of the shroud on the onset of the vortex ring state. The notional induced velocity of the shrouded rotor's wake, at the shroud outlet plane, was used to scale the descent velocity of both investigations performed.

In hover, the average velocity profiles extracted at the shroud outlet indicated that the adopted shroud did not significantly affect the mean axial velocity profile produced by the rotor. In contrast to the isolated rotor, where the flow field is dominated by the blade root and tip vortices, POD analysis showed that the most probable and energetic

realisation of the fluctuations of the flow field manifests itself as the radial flapping of the shrouded rotor's wake.

At low descent velocities, $\alpha \leq 1.0$, a large region of recirculation forms outboard of the shroud. As the descent velocity increased, the recirculation moved from upstream of the shroud to around the side of the shroud, as the rotor enters the VRS. At higher velocity ratios, the shrouded rotor entered a state analogous to the windmill brake state of an isolated rotor. In the windmill brake state, the wind-tunnel free stream penetrates through the shroud outlet plane and passes around the shroud. The flow topology produced by the shrouded rotor is generally similar to that produced by the isolated counterpart in axial descent. However, the velocity profiles at the shroud outlet plane and the recording of the position of the mean stagnation point originating from the interaction between the rotor wake and the wind-tunnel free stream suggest that the presence of the shroud might slightly delay the onset of the VRS.

The flow field produced by a shrouded rotor operating in axial descent is highly unsteady and the recirculation aperiodically sheds away from the shroud. POD showed that most of the flow unsteadiness associated with the VRS is caused by

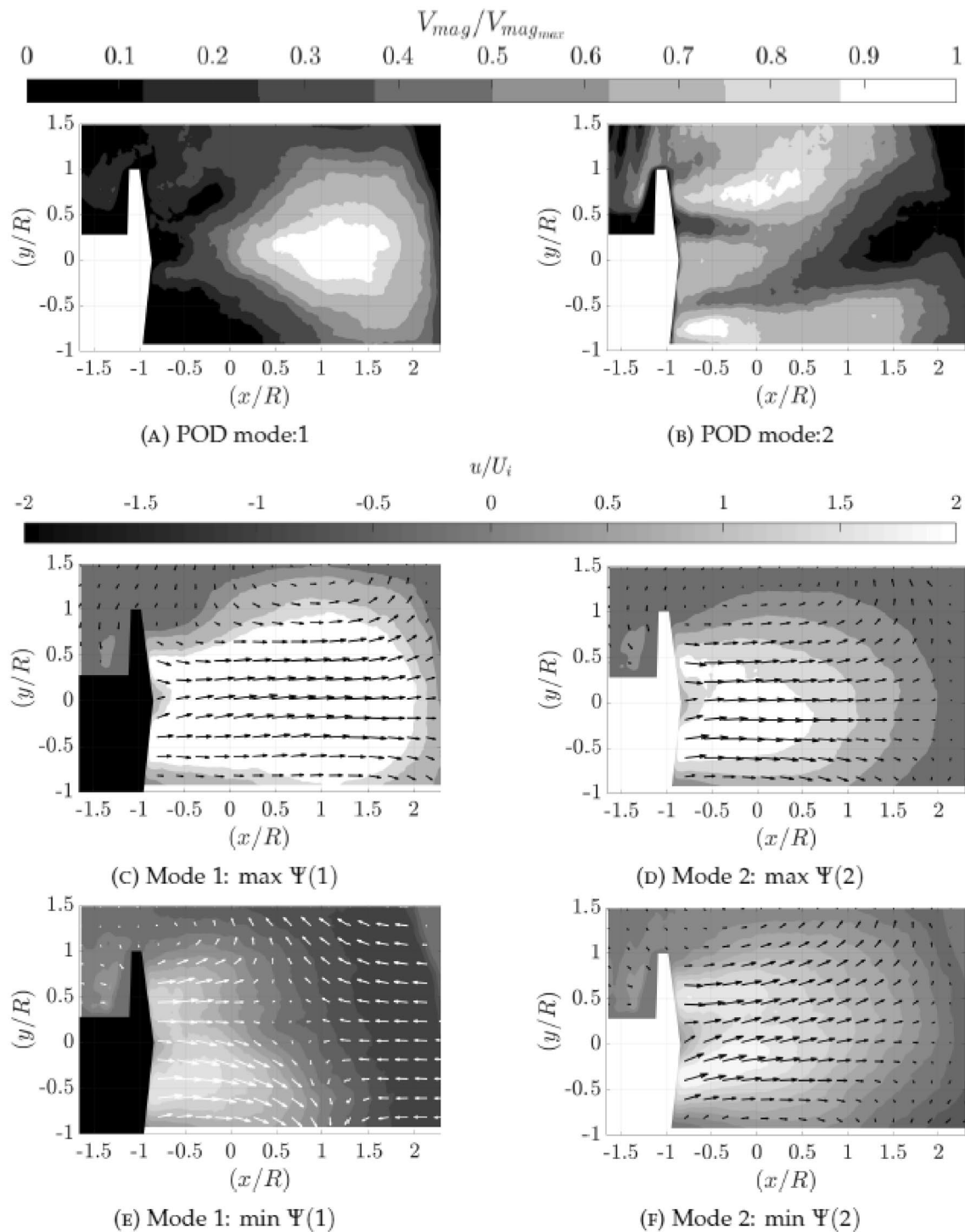


Fig. 21 Visualisation of the first two POD eigenmodes of the velocity fluctuations produced by a isolated rotor $\alpha = 1.0$ calculated from 600 instantaneous velocity fields. **A** mode 1, **B** mode 2. The vector lengths are scaled with respect to the maximum vector length of each

individual mode. Reconstructed simulations of the velocity field produced by the subtraction of the maximum (**C, D**) and minimal (**E, F**) reconstruction coefficient representations of the first two modes from the mean field are presented in this figure

the variation of the wake penetration into the free stream flow. The location of these fluctuations mostly coincides with a region of high RMS of the axial velocity, which is of the order

of the notional induced velocity. In this condition, the flow can penetrate up to the shroud outlet plane and the location of the stagnation point varies as a result of the flow fluctuations.

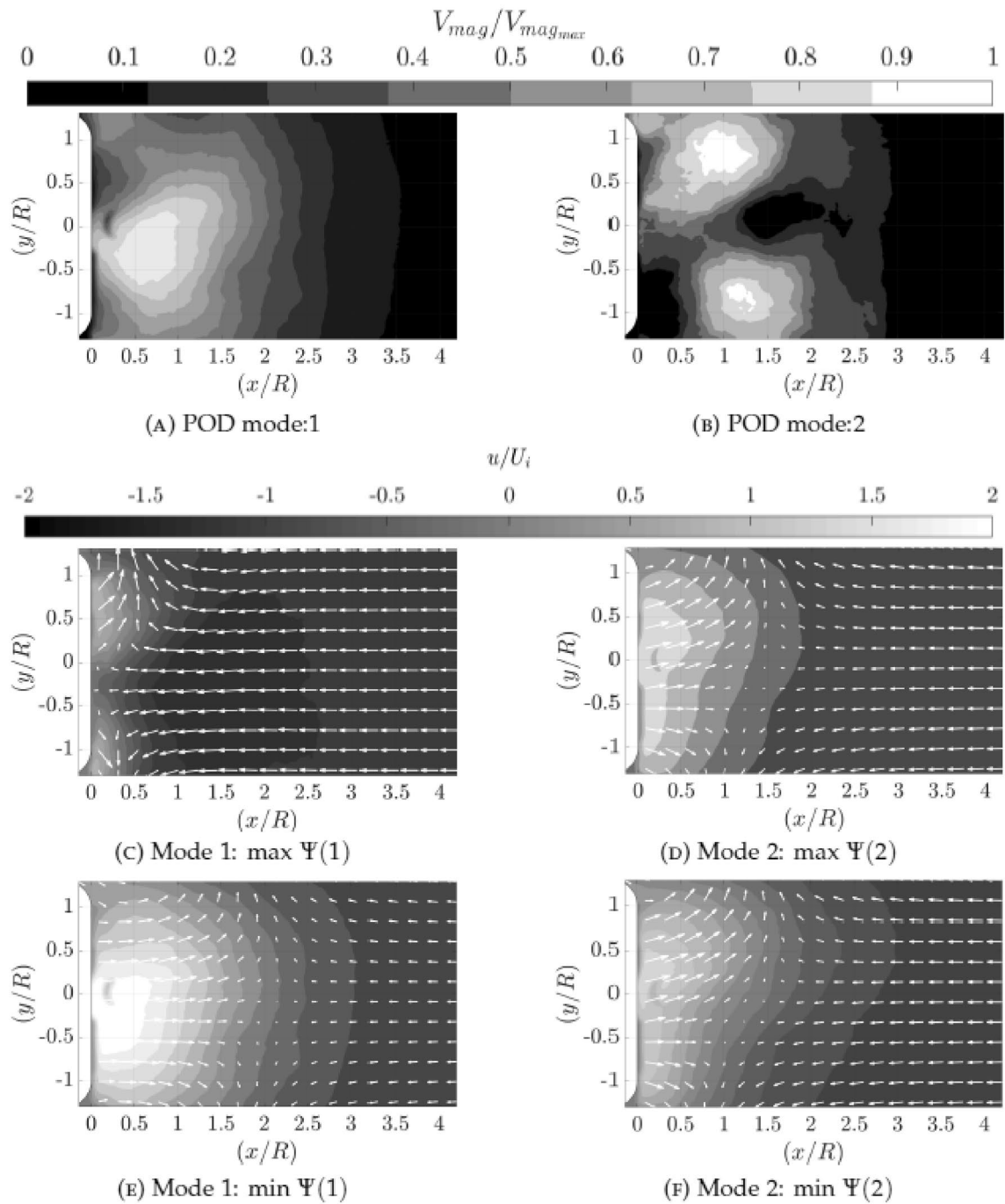


Fig. 22 Visualisation of the first two POD eigenmodes of the velocity fluctuations produced by the shrouded rotor $\alpha = 1.1$ calculated from 600 instantaneous velocity fields. **A** mode 1, **B** mode 2. The vector lengths are scaled with respect to the maximum vector length of each

individual mode. Reconstructed simulations of the velocity field produced by the subtraction of the maximum (**C**, **D**) and minimal (**E**, **F**) reconstruction coefficient representations of the first two modes from the mean field are presented in this figure

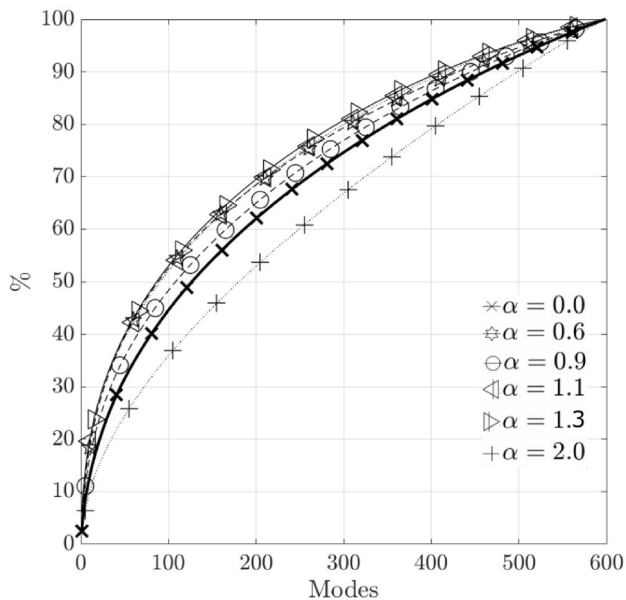


Fig. 23 Progressive sum of singular values as a percentage of the total sum calculated from the POD of the flow field produced by the shrouded rotor operating at several values of α

Author Contributions DP was involved in conceptualisation, data analysis, investigation, methodology, visualisation, writing (original draft), writing (review & editing). DZ contributed to data analysis, investigation, methodology, writing (original draft), writing (review & editing). AB was involved in supervision, writing (original draft), writing (review & editing). RBG contributed to conceptualisation, funding acquisition, investigation, methodology, supervision, visualisation, writing (original draft), writing (review & editing)

Funding The work was funded by the EPSRC. Acknowledgement is given to the National Wind Tunnel Facility, EPSRC Grant Number EP/L024888/1. for the provision of experimental equipment.

Data Availability Data and further information are available upon request, please contact the corresponding author.

Declarations

Conflict of interest The authors have no conflicts of interest to declare, either financial or non-financial, that are relevant to the content of this article.

Ethical approval Not applicable.

Open Access This article is licensed under a Creative Commons Attribution 4.0 International License, which permits use, sharing, adaptation, distribution and reproduction in any medium or format, as long as you give appropriate credit to the original author(s) and the source, provide a link to the Creative Commons licence, and indicate if changes were made. The images or other third party material in this article are included in the article's Creative Commons licence, unless indicated otherwise in a credit line to the material. If material is not included in the article's Creative Commons licence and your intended use is not permitted by statutory regulation or exceeds the permitted use, you will

need to obtain permission directly from the copyright holder. To view a copy of this licence, visit <http://creativecommons.org/licenses/by/4.0/>.

References

- Akturk A, Shavaliqul A, Camci C (2009) PIV measurements and computational study of a 5-inch ducted fan for V/STOL UAV applications. In: 47th AIAA Aerospace sciences Meeting and Exhibit, Orlando, Florida
- Albrecht HE, Borys M, Damaschke N, Tropea C (2013) Laser doppler and phase doppler measurement techniques. Berlin, Springer Science and Business Media
- Ananthan S, Leishman JG (2006) Rotor wake aerodynamics in large amplitude maneuvering flight. *J Am Helicopter Soc* 51(3):225–243
- Berbero S (2000) A turbulent jet in counterflow. PhD thesis. Berlin: Technical University Of Berlin
- Bhagwat JM, Leishman GJ (2000) Stability analysis of helicopter rotor wakes in axial flight. *J Am Helicopter Soc* 45(3):165–178
- Black DM, Wainauski HS, Rohrbach C (1968) Shrouded propellers - a comprehensive performance study. In: AIAA 5th Annual Meeting and Technology Display, Philadelphia
- Bothezat GD (1919) The general theory of blade screws. NACA report no29
- Brinson P (1998) Experimental investigation of the vortex ring condition. In: 24th European Rotorcraft Forum, Marseille
- Brotherhood P (1949) Flow through a helicopter rotor in vertical descent. Aeronautical Research Committee, R &M No2735
- Colin Y, Bertrand B, Patron T, Phoi V (2016) Quadcopter. US Patent No US D747,775 S
- Drees JM, Hendl WP (1951) Airflow patterns in the neighbourhood of helicopter rotors: A description of some smoke tests carried out in a wind-tunnel at Amsterdam. *J Aircr Eng Aerosp Technol* 23(266):107–111
- George WK (1988) Quantitative measurement with the burst-mode laser doppler anemometer. *J Exp Therm Fluid Sci* 1(1):29–40
- Graf W, Fleming J, Ng W (2008) Improving ducted fan UAV aerodynamics in forward flight. In: 46th AIAA Aerospace Sciences Meeting and Exhibit p 430
- Green RB, Gillies EA, Brown RE (2005) The flow field around a rotor in axial descent. *J Fluid Mech* 534:237–261
- Gupta BP, Loewy RG (1974) Theoretical analysis of the aerodynamic stability of multiple, interdigitated helical vortices. *AIAA J* 12(10):1381–1387
- Hamel G (1923) Aeroplane. US Patent No 1,463,694
- Heller H (1997) Into the physics of rotor aeroacoustics—highlights of recent european helicopter noise research. In: Fifth international congress on sound and vibration
- Hubbard HH (1950) Sound measurements of five shrouded propellers at static conditions. NACA-TN-2024
- Krüger W (1949) On wind tunnel tests and computations concerning the problem of shrouded propellers. Tech Report, National Advisory Committee for Aeronautics
- Leishman GJ, Bhagwat MJ, Ananthan S (2004) The vortex ring state as a spatially and temporally developing wake instability. *J Am Helicopter Soc* 49(2):160–175
- Martin P, Tung C (2004) Performance and flowfield measurements of a 10-inch ducted rotor VTOL UAV. In: American Helicopter Society 60th Annual Forum Proceedings, Baltimore
- Mouille R (1970) The Feneston shrouded tail rotor of the SA.341 Gazelle. *J Am Helicopter Soc* 15(4):31–37

- Patter-Rouland B, Lalizel G, Moreau J, Rouland E (2001) Flow analysis of an annular jet by particle image velocimetry and proper orthogonal decomposition. *Meas Sci Technol* 12:1404–1412
- Pereira JL (2008) Hover and wind-tunnel testing of shrouded rotors for improved micro air vehicle design. PhD Thesis
- PIVTechGmbH (2019) PIVpart160 product information. <https://www.pivtec.com/>, Last accessed on 14/04/2019
- Raffel M, Willert C, Wereley S, Kompenhans J (2007) Particle Image Velocimetry. A Practical Guide, 2nd edn. Berlin, Springer
- Reeder JP, Gustafson FB (1949) On the flying qualities of helicopters. NACA-TN-D-1799
- Ryu M, Cho L, Cho J (2017) The effect of tip clearance on performance of a counter-rotating ducted fan in a vtol uav. *Japan Soc* 60(1):1–9
- Savas O, Green RB, Caradonna FX (2009) Coupled thrust and vorticity dynamics during vortex ring state. *J Am Helicopter Soc* 54(2):22001
- Taira K, Brunton SL, Dawson STM, Rowley CW, Colonius T, McKeon BJ, Schmidt O, Gordeyev S, Theofilis V, Ukeiley LS (2017) Modal analysis of fluid flows: an overview. *AIAA J* 55(12):4013–4041
- Taylor RT (1958) Experimental investigation of the effect of some shroud design variables on the static thrust characteristics of a small-scale shrouded propeller submerged in a wing. NACA-TN-4126
- Vuillet A, Morelli F (1986) New aerodynamic design of the fenestron for improved performance. In: 12th European Rotorcraft Forum, Garmisch-Partenkirchen, Federal Republic of Germany, Paper No 8
- Young L, Aiken E, Johnson J, JRDA (2002) New concepts and perspectives on micro-rotorcraft and small autonomous rotary wing vehicles. In: AIAA Applied Aerodynamics Conference, St Louis
- Zhang Z (2010) LDA Application Methods: Laser Doppler Anemometry for Fluid Dynamics. Springer, Berlin

Publisher's Note Springer Nature remains neutral with regard to jurisdictional claims in published maps and institutional affiliations.